La$_{1.5}$Sr$_{0.5}$NiMn$_{0.5}$Ru$_{0.5}$O$_6$ Double Perovskite with Enhanced ORR/OER Bifunctional Catalytic Activity

Maria Retuerto[1*], Federico Calle-Vallejo[2], Laura Pascual[3], Gunnar Lumbeeck[4], María Teresa Fernandez-Diaz[5], Mark Croft[6], Jagannatha Gopalakrishnan[7], Miguel A. Peña[1], Joke Hadermann[4], Martha Greenblatt[8], Sergio Rojas[1*]

[1] Grupo de Energía y Química Sostenibles, Instituto de Catálisis y Petroleoquímica, CSIC. C/ Marie Curie 2, L10. 28049, Madrid, Spain.

[2] Departament de Ciència de Materials i Química Fisica & Institut de Química Teòrica i Computacional (IQTCUB), Universitat de Barcelona, Martí i Franqués 1, 08028 Barcelona, Spain

[3] Instituto de Catálisis y Petroleoquímica, CSIC. C/ Marie Curie 2, L10. 28049, Madrid, Spain.

[4] EMAT, University of Antwerp, Groenenborgerlaan 171, 2020 Antwerp, Belgium

5 Institut Laue-Langevin, BP156X, Grenoble, F-38042, France.

6 Department of Physics, Rutgers, The State University of New Jersey, 610 Taylor Road, Piscataway, New Jersey, 08854, USA

7 Solid State and Structural Chemistry Unit, Indian Institute of Science, Bangalore 560 012, India.

8 Department of Chemistry and Chemical Biology, Rutgers, The State University of New Jersey, 610 Taylor Road, Piscataway, New Jersey, 08854, USA

Corresponding Authors

* srojas@icp.csic.es, m.retuerto@csic.es

Table of Contents

S1. X-Ray Powder Diffraction

Figure S1 shows the Rietveld refinement of the structure of $La_{1.5}Sr_{0.5}NiMn_{0.5}Ru_{0.5}O_6$ (LSNMR) in $P2_1/n$ space group by x-ray diffraction.
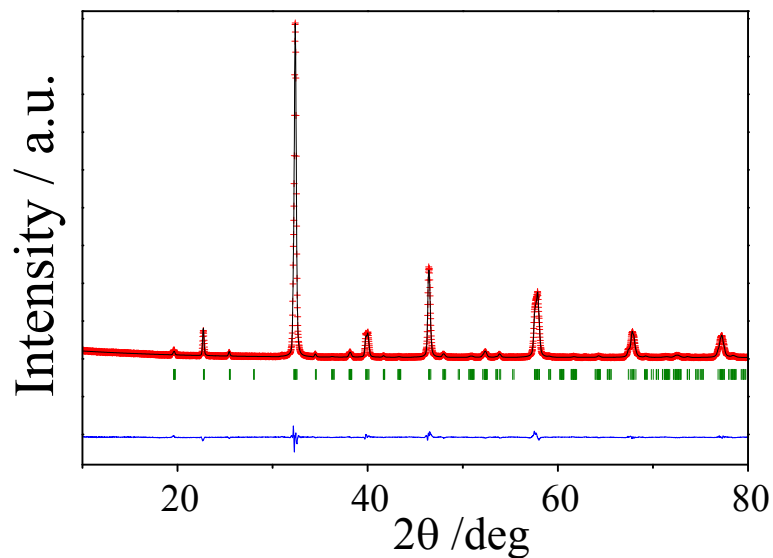
Figure S1. XRD Rietveld profiles of the structure of $La_{1.5}Sr_{0.5}NiMn_{0.5}Ru_{0.5}O_6$, LSNMR, refined with the $P2_1/n$ monoclinic space group. Crosses are the observed pattern, the black full line is the calculated one and the bottom blue line is the difference between both. The green lines indicate the Bragg reflections of the selected space group.

S2. Electron Diffraction
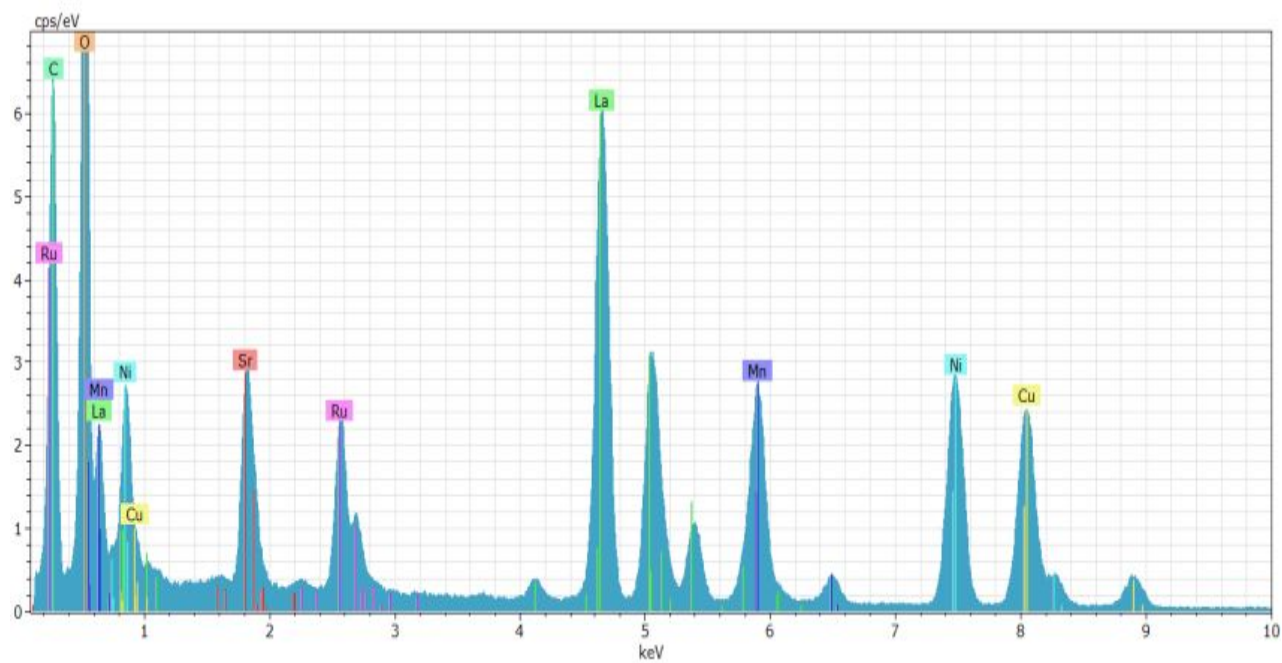
Figure S2. Representative EDX spectrum of LSNMR to illustrate the composition obtained.
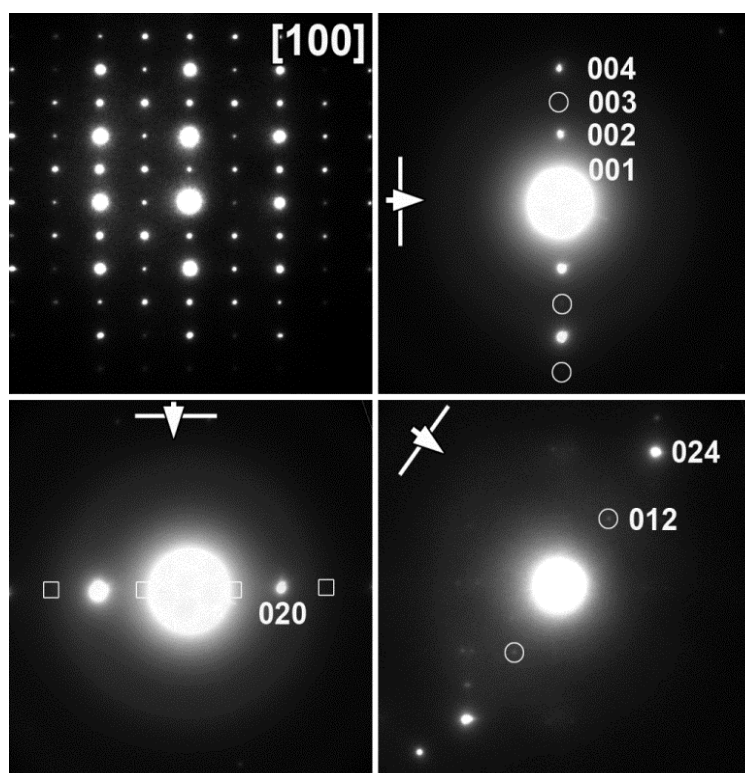
Figure S3. Selected Area Electron Diffraction (SAED) of LSNMR indexed in a perovskite cell.

As shown in Figure S3, by tilting around the relevant rows of reflections, the 0k0: k = 2n+1 reflections (indicated by squares) are due to double diffraction, since they disappear when removing the possible double diffraction paths, while 00l: l = 2n+1 (indicated by circles in the top right pattern) are not due to double diffraction. We investigated whether the [100] patterns could actually be twinned patterns of [100] with 0kl: k = 2n and [010] with h0l: h+l = 2n, with the 0kl: k = 2n+1, l = 2n being due to double diffraction only. This is necessary since this would exactly correspond to Pbnm (or in the conventional setting for perovskites Pnma with a ≈ √2a_p, b ≈ 2a_p, c ≈ √2a_p), which has the same octahedral tilt pattern as P$2_1/n$ but without cation order. The tilt around the 0kl: l = 2k row of reflections, shown also in Figure S3 (indicated by circles in the bottom right pattern), show that these reflections remain present even when all double diffraction paths to these reflections are eliminated. This proves that these reflections are not due to double diffraction on top of a twinned pattern, but that there is indeed no reflection condition for 0kl reflections. Therefore, only P$2_1/n$ is in agreement with the experimental electron diffraction results.

S3. Powder Neutron Diffraction

Table S1. Atomic parameters after the refinement of the crystallographic structure of $La_{1.5}Sr_{0.5}NiMn_{0.5}Ru_{0.5}O_6$ from high resolution PND data at T = 295 K. Space group $P2_1/n$. Lattice parameters: a = 5.5458(3) Å, b = 5.5035(3) Å, c = 7.7985(4) Å, ß = 89.95(1)° and V = 238.02(2) Å³. Discrepancy factors: R_p = 2.38%, R_{exp} = 2.17%, R_{wp} = 3.07% and R_{Bragg} = 5.57%, χ^2 = 1.99.

Atom	Site	x	y	z	f_{occ}	B(Å²)
La/Sr	*4e*	0.0032(8)	0.0213(5)	0.2518(9)	0.75/0.25	0.12(4)
Ni/Ru	*2a*	1/2	0	1/2	0.5/0.5	0.17(5)
Ni/Mn	*2b*	1/2	0	0	0.5/0.5	0.17(5)
O1	*4e*	0.2937(9)	0.2796(11)	0.0322(9)	1.000	0.01(4)
O2	*4e*	0.2429(9)	0.7634(9)	0.0320(8)	1.000	0.01(4)
O3	*4e*	-0.0690(7)	0.4909(8)	0.26120(9)	1.000	0.01(4)

Table S2. Atomic distances (Å) for Ni/RuO_6 and Ni/MnO_6 octahedra and selected bond angles (°) at 295 K.

Description	Bond distance
Ni/Ru – O1 (x2)	2.046(5)
Ni/Ru – O2 (x2)	1.995(5)
Ni/Ru – O3 (x2)	2.073(6)
< Ni/Ru – O>	2.038(2)
Ni/Mn – O1 (x2)	1.934(6)
Ni/Mn – O2 (x2)	1.947(5)
Ni/Mn – O3 (x2)	1.902(6)
< Ni/Mn – O >	1.928(2)

Description	Angle
(Ru/Ni-O1-Mn/Ni)	157.9(2)
(Ru/Ni-O2-Mn/Ni)	164.7(2)
(Ru/Ni-O3-Mn/Ni)	157.6(3)

S4. X-ray absorption near edge spectroscopy (XANES)

S4.1. Ni-K and Mn-K pre-edges

The 3d row transition metal pre-edge features are due to quadrupole-allowed transitions into final d-states or into hybridization-allowed dipole transitions into d/ligand-p states. Those are shifted below the main edge by the final state d-electron/core-hole Coulomb interaction. The spectral shape, intensity, and chemical shift of the pre-edge features can also be used as valence indicators.[1-3] In the case of the Ni-K pre-edge, doping studies have shown a systematic increase in pre-edge feature intensity and chemical shift for Ni valences in the 2+ to 3.3+ range.[1] In Figure S4a, the Ni-K pre-edge of LSNMR exhibits a low chemical shift and spectral area (close to $La_2Ni^{2+}VO_6$). Thus, both the Ni-K main edge and pre-edge results support Ni^{2+} configuration in LSNMR.
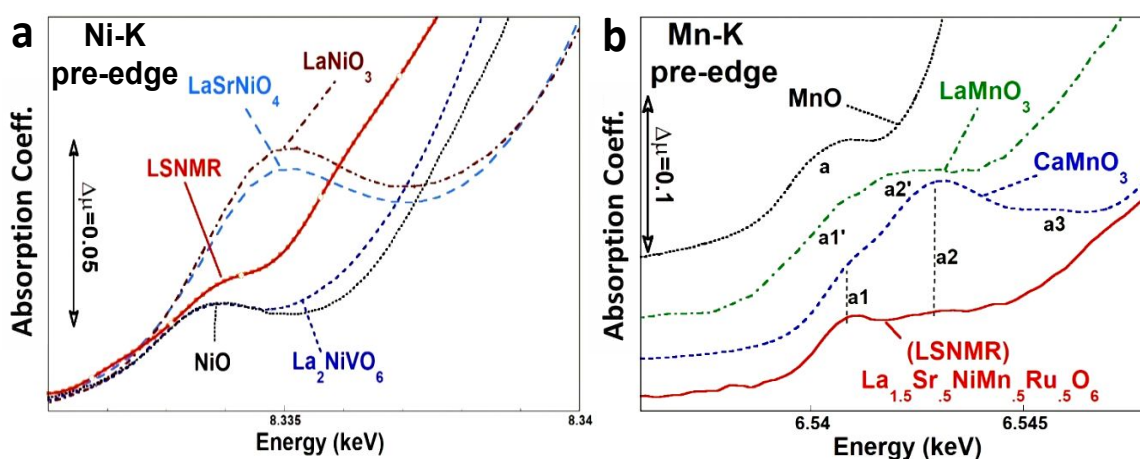
**Figure S4(a).** Ni-K pre-edge spectra for LSNMR and the standard compounds: ~Ni^{2+} standards NiO and La_2NiVO_6; and ~Ni^{3+} standards $LaNiO_3$ and $LaSrNiO_4$. **(b)** Mn-K pre-edge spectra for LSNMR and the standard compounds: ~Mn^{2+}, MnO; ~Mn^{3+}, $LaMnO_3$; and ~Mn^{4+}, $CaMnO_3$. Note the standard spectra have been displaced vertically for clarity and nominal pre-edge features are identified.

Figure S4b compares the Mn-K pre-edge of LSNMR to those of standard Mn compounds. It should be noted that a1-a2 features for the Mn^{4+} standard are shifted up in energy relative to the a1'-a2' features in the Mn^{3+} standard. The a1-a2 features for LSNMR are similar in energy (albeit less intense) to the Mn^{4+} standard. Thus the Mn-K pre-edge feature structure and intensity only supports a Mn valence well above 3+.

S4.2. 4d-L₃ edges

Figure S5 shows the systematic M(4d)-L_3 edge variation with 4d-count for octahedral ligand coordination. The $L_{2,3}$-edges of transition metals are dominated by intense "white line" (WL) spectral features at the edge onsets.[3-6] These WL-features are due to transitions

into empty d final states and can be used as a probe of the d occupancy through both their spectral distribution and chemical shift. In the case of $4d$ transition metal compounds, with octahedral ligand coordination, the $4d$-orbitals are split into a lower lying 6-fold-degenerate t_{2g} and excited 4-fold-degenerate e_g states. To first-order this ligand field splitting is reflected in a splitting of the 4d-$L_{2,3}$-edge WL-features in such compounds into a bimodal A(t_{2g} related)/B(e_g related) structure (see the A and B features and Figure S5). This splitting is illustrated in Figure S5 for the L_3 edges of 4d-row perovskite related compounds.[3-6] It should be noted that the intensity of the A(t_{2g} related) feature systematically decreases, relative to the B(e_g related) feature, as the 4d configuration increases from $4d^0$ to $4d^4$ (i.e. as the t_{2g} hole count decreases from 6 to 2). It is worth noting that while the ligand field split levels and systematic 4d-occupation trends are apparent in such compounds, multiplet and spin orbit interaction effects can also be discerned in 4d-row compounds.[5]
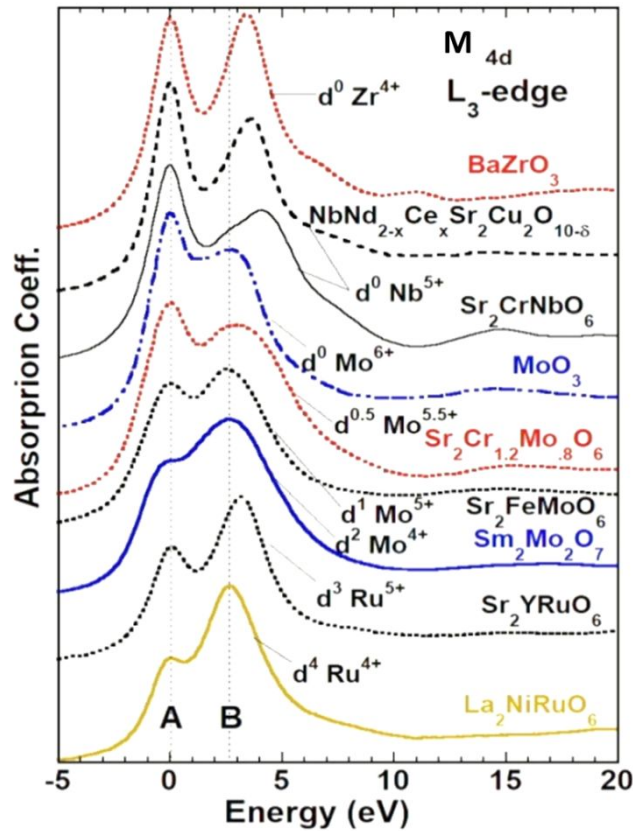
Figure S5. The M-L_3 edges of a series of T_{4d} compounds (with octahedral O-ligand symmetry), T_{4d} = Zr, Nb, Mo, and Ru, with d-occupancies varying from d^0 to d^4. For comparison, the spectra have been nominally aligned to the A-(t_{2g} related) feature. Note the systematic decrease in the A-feature intensity, relative to the B-(e_g related) feature as the d-count increases (i.e. as the d final state hole count decreases).

The first conclusion of the XANES is that it supports the LSNMR formula with the nominal formal valences of Ni^{2+}-Mn^{4+}-Ru^{5+}, with the caveat that integral valence states in the solid-state environment are a substantial oversimplification. A configuration of the Ni^{2+} is strongly supported. A configuration of close to Mn^{4+} is evidenced with a quantitative estimate of $Mn^{3.7+}$ being motivated by main-edge peak position. A configuration of close to Ru^{5+} is evidenced, but with the possibility of a somewhat smaller value based upon the chemical shift.

The main-edge evidence for the more precise estimate of $Mn^{3.7+}$ does have an empirical basis and should be noted. In this regard it is worth noting that the weighted average of the SEM and TEM stoichiometries [$La_{0.80(3)}Sr_{0.24(3)}Ni_{0.5(1)}Mn_{0.27(3)}Ru_{0.22(8)}O_x$] would almost precisely agree with Ni^{2+} - $Mn^{3.7+}$ - Ru^{5+} if x = 3. In view of the uncertainties, this stoichiometry/Mn-valence is likely fortuitous, but it emphasizes that the question of a possible Mn-valence somewhat lower than 4+ in LSNMR must remain open. The evidence for a Ru-valence slightly less than 5+ is less strong, but should also be considered an open question.

S5. Electrochemical Performance

S5. 1. Electrochemical impedance spectroscopy (EIS)
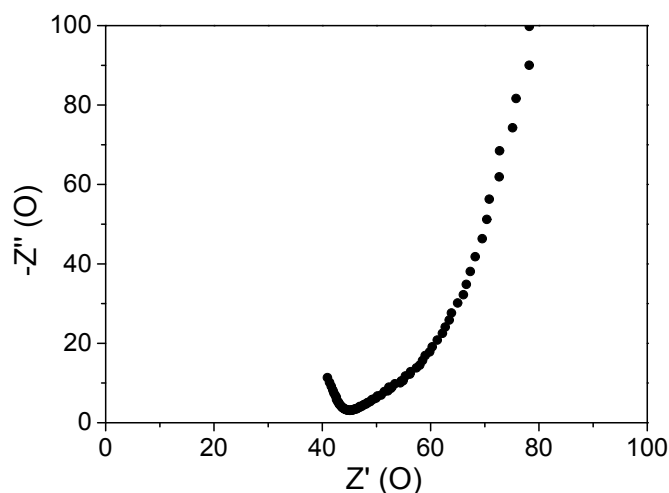
Figure S6. Nyquist plot of LSNMR from an electrochemical impedance spectroscopy experiment at open voltage.

### S5.2. RRDE measurement to determine the production of H_2O_2 during the ORR.

The ORR can proceed via 4 electrons ($O_2 \rightarrow H_2O$) or 2 electrons ($O_2 \rightarrow H_2O_2$) and the relative production of H_2O_2 was assessed using a RRDE with a Pt ring at 1.2 V during the ORR reaction. At 1.2 V, the H_2O_2 eventually formed during the ORR, produces O_2 at the Pt ring, giving oxidizing currents. The H_2O_2 fraction formed is calculated from the formula:

$$X_{H_2O_2} = \frac{\frac{2i_R}{N}}{i_D + \frac{i_R}{N}} \tag{S1}$$

where i_D is the current obtained at the disk and i_R is the current obtained at the Pt ring. N is the ring's efficiency, set at 26 %. The number of exchanged electrons is then calculated from:

$$ne = 4 - \left(\frac{\%H_2O_2}{50\%}\right) \tag{S2}$$

The RRDE measurement (Figure S7) shows that 6% of the product obtained during ORR is H_2O_2.
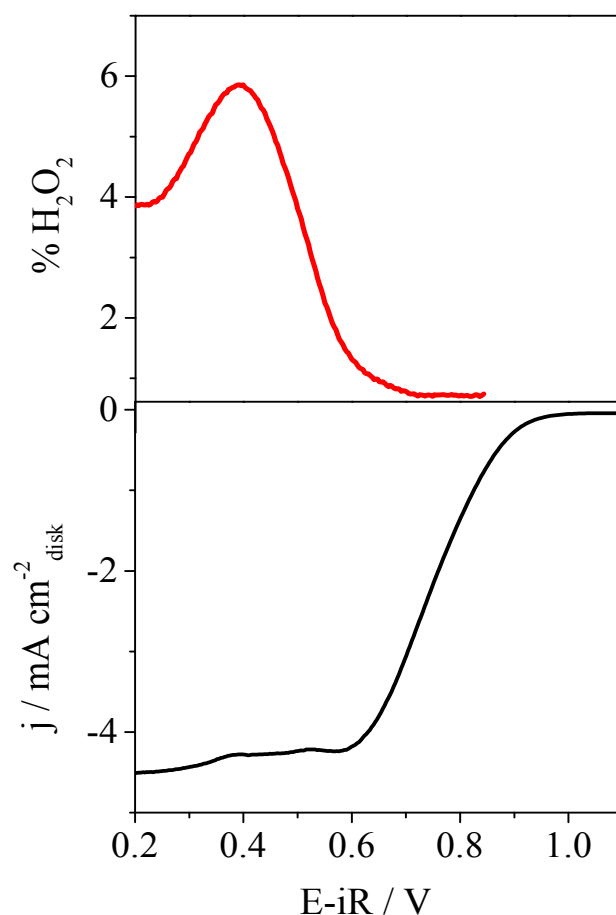
Figure S7. RRDE ORR measurement with the Pt ring settled at 1.2 V.

S5.3. ECSA

The electrochemically active surface area (ECSA) was calculated by the double-layer capacitance of LSNMR without active carbon. We performed cyclic voltammograms at different velocities close to the "*open circuit potential*" in Ar, where it is suppose that the measured currents are due to double-layer charging. ECSA was recorded at 200, 100, 50, 20 and 10 mV/s between 0.78 and 0.98 V *vs.* RHE (Figure S8). The double-layer charging current would be equal to the product of the scan rate (v) and the double-layer capacitance (C_{dl}) as $i_c= vC_{dl}$. If i_c is plotted as a function of v, then the slope will be C_{dl}, and ECSA will be ECSA= C_{dl}/ C_S; where C_S is the specific capacitance of an atomically flat planar surface of the material per unit area under identical electrolyte conditions. Since this value is not well established for oxides we used 0.06 mF/cm^2, used in several references for 0.1M KOH.[7] The ECSA obtained was 2 cm^2.
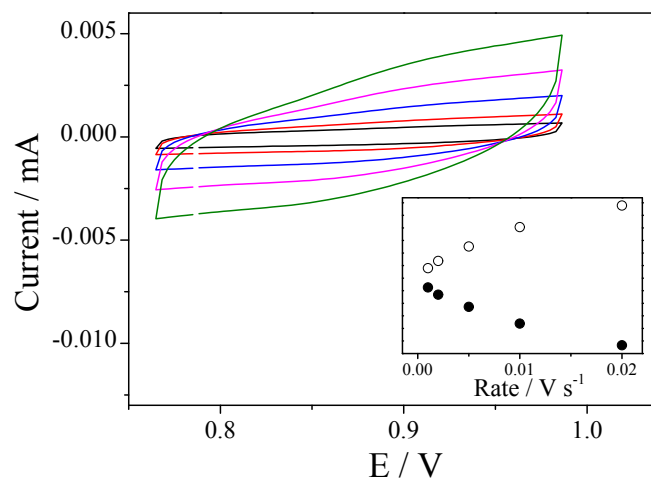
Figure S8. ECSA calculations of LSNMR.

S5.4. Intrinsic Activity

Intrinsic activities (i_s in mAcm$^{-2}_{oxide}$) were calculated by normalizing i_f to the actual specific surface area of the oxide deposited on the electrode with the following equation:

$$i_s = \frac{i_f}{(g_{oxide}xBET_{oxide})} \tag{S3}$$

where BET$_{oxide}$ is the specific surface area of LSNMR, namely 2 m²/g, obtained from the BET measurements.
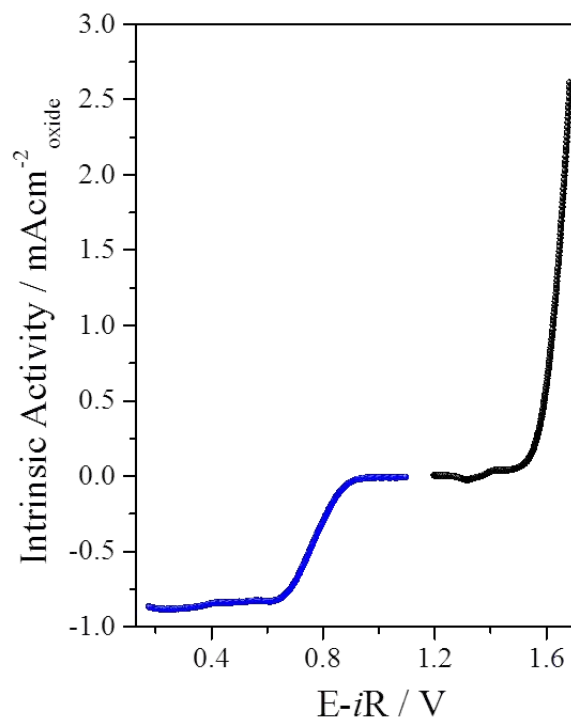
Figure S9. ORR and OER Intrinsic Activities of LSNMR.

S5.5. ORR Kinetic current and Mass Activity.

ORR kinetic current (i_k) are calculated from the Koutecky–Levich equation:

$$i_k = -\frac{i_F \times i_{lim}}{i_F - i_{lim}} \tag{S4}$$

where i_F is the Faradaic current and i_{lim} is the limiting current. Using the kinetic current we calculate the mass activity of LSNMR (Figure 3b of the main text):

$$i_m = -\frac{i_k}{g_{oxide}} \tag{S5}$$

.6. RRDE measurement to determine the production of O_2 during the OER.

We performed RRDE measurement during the OER in an electrolyte free of O_2, with the Pt ring settled at 0.4 V. At this potential the O_2 produced during the OER reaction will be reduced on the Pt ring and give a reducing current (see Figure S10).
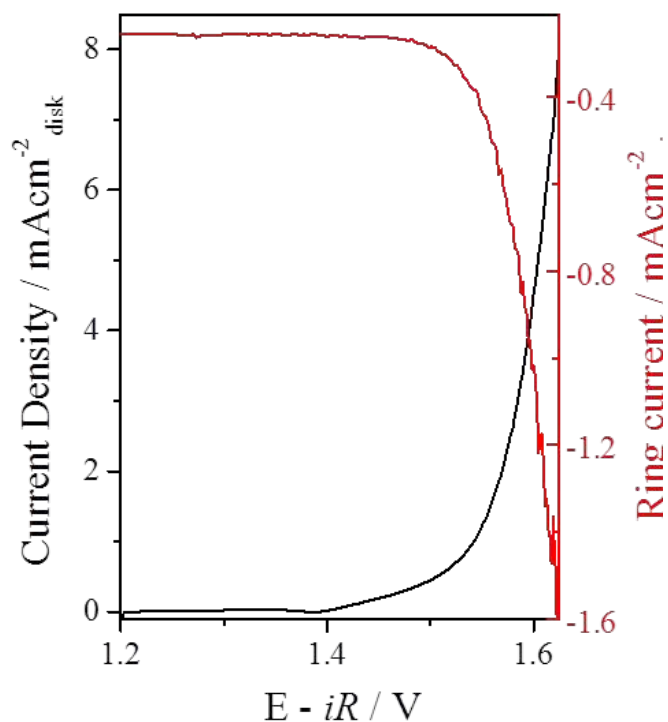
Figure S10. RRDE OER measurement with the Pt ring settled at 0.4 V to observe the reduction of the O_2 formed during the OER reaction.

S6. BET Surface Area

BET Surface Area
BET Surface Area: 2.0179 ± 0.0096 m²/g
Slope: 2.143453 ± 0.010163 g/cm³
Y-Intercept: 0.013880 ± 0.001657 g/cm³

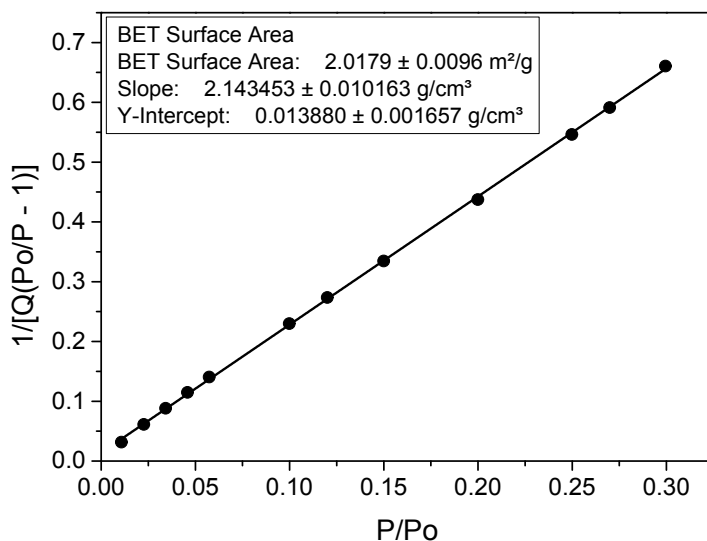**Figure S11:** $La_{1.5}Sr_{0.5}NiMn_{0.5}Ru_{0.5}O_6$ BET surface area plot.

S7. Computational Details

We performed the DFT calculations with VASP,[8] with the projector augmented wave (PAW) approach,[9] the GGA-PBE exchange-correlation functional,[10] and Dudarev's DFT+U formalism[11] with U_{eff} values of 6.01 eV for Ni, 4.46 for Mn, and 6.70 for Ru ions. For Ni and Mn the values used are the average of those reported by Ceder and co-workers[12] for various Ni- and Mn-containing compounds. For Ru we used the value reported by Xu et al.[13]

We used 2×2 (001) perovskite slabs to simulate the surfaces (4 atomic layers thick: atoms in the topmost two layers and the adsorbates were fully relaxed, whereas the bottommost two were fixed at the equilibrium bulk distances, please refer to Figure S12), which contained four formula units in each case, with 4×4×1 k-point grids and a plane-wave cutoff of 450 eV. We added ~15 Å of vacuum in the z direction to avoid interactions between periodically repeated slabs. As shown in previous works, this setup suffices for the adsorption energies to be converged within 0.05 eV.[14-16]
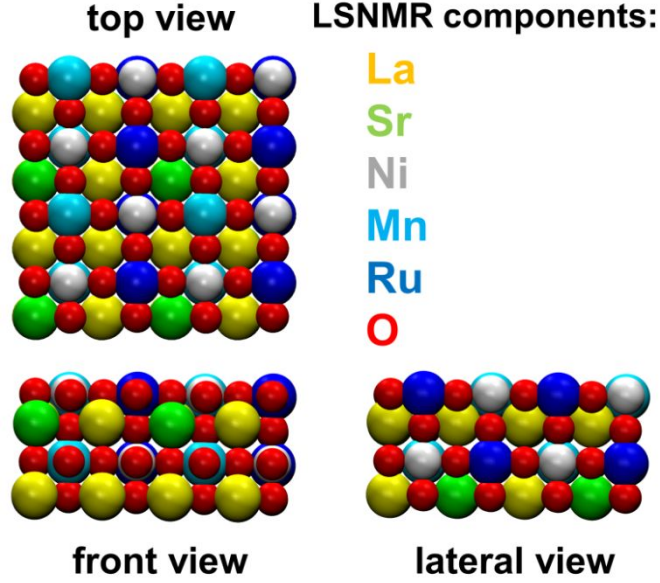
Figure S12. Top, front and side views of the LSNMR slabs under study. The colour code for each component is provided in the figure.

The calculations were made spin unrestricted in all cases. The relaxations were made with the conjugate-gradient scheme with k_BT = 0.01 eV and Gaussian smearing, taking the energies extrapolated to 0 K, until the maximal force on the relaxed atoms was 0.05 eV/Å. H_2O and H_2 were calculated in boxes of 15 Å × 15 Å × 15 Å and a 1×1×1 k-point grid with k_BT = 0.001 eV. The Gibbs energies were approximated as: $G \approx E_{DFT} + ZPE - TS$, where E_{DFT} and ZPE are the DFT-calculated total and zero-point energies respectively, while TS are entropic corrections for fluid-phase species. For $H_2O(l)$ and $H_2(g)$ the TS corrections are 0.67 and 0.40 at 298.15 K,[17] while the $ZPEs$ for H_2O and H_2 are 0.58 and 0.28 eV.[17] The $ZPEs$ for *O, *OH and *OOH are 0.07, 036 and 0.43 eV.

To describe the energetics of $(H^+ + e^-)$ in terms of $\frac{1}{2}H_2(g)$ we used the computational hydrogen electrode.[18] Details on the construction of scaling-relation-based volcano plots appear elsewhere.[19] We assume that the OER mechanism is $OH^- \rightarrow *OH \rightarrow *O \rightarrow *OOH \rightarrow O_2$. The OER overpotential is calculated as:

$$\eta_{OER} = \max\left(\Delta G_1, \Delta G_2, \Delta G_3, \Delta G_4\right)/e - E^0 \tag{S6}$$

where $\Delta G_1 = \Delta G_{OH}$, $\Delta G_2 = \Delta G_O - \Delta G_{OH}$, $\Delta G_3 = \Delta G_{OOH} - \Delta G_O$, $\Delta G_4 = 4E^0 - \Delta G_{OOH}$, and $E^0 = 1.23$ V is the equilibrium potential of the reaction. Note that ΔG_O is the reaction energy of $* + H_2O \rightarrow *O + 2H^+ + 2e^-$, ΔG_{OH} is the reaction energy of $* + H_2O \rightarrow *OH + H^+ + e^-$, and ΔG_{OOH} is in turn the reaction energy of

$* + 2H_2O \rightarrow *OOH + 3H^+ + 3e^-$. From the acid-based reference of the adsorption energies to the alkaline one is based on the reaction $H_2O \rightarrow H^+ + OH^-$, which has a free energy of 0.83 eV. Note that the use of either scale has no influence on the predicted overpotentials. The electrochemical-step symmetry index (ESSI) is defined as follows for the OER:[20]

$$ESSI = \left(\frac{1}{n} \sum_i^n \Delta G_i^* \right) - E^0 \qquad (S7)$$

where ΔG_i^* are the adsorption energies in ΔG_1 to ΔG_4 larger than $E^0 = 1.23$ V. For instance, the adsorption energies of *O, *OH, and *OOH for Ru sites at LSNMR (Ru @ LSNMR) are 2.27, 0.54, and 3.89 eV, according to Table S3. 0.54, 1.73, 1.62 and 1.03 eV, so that the overpotential is $\eta_{OER}^{LSNMR} = 1.73 - 1.23 = 0.50$ V and $ESSI_{OER}^{LSNMR} = (1.73 + 1.62)/2 - 1.23 = 0.44$ V.

If the ORR is assumed to proceed as: $O_2 \rightarrow *OOH \rightarrow *O \rightarrow *OH \rightarrow OH^-$, one can make an analogous analysis so as to be able to calculate η_{ORR}, $ESSI_{ORR}$[20] and the bifunctional index as:

$$BI = \eta_{OER} + \eta_{ORR} \qquad (S8)$$

Table S3 contains ΔG_O, ΔG_{OH}, ΔG_{OOH}, $ESSI_{OER}$, $ESSI_{ORR}$, η_{OER} and η_{ORR} for the different sites on LSNMR.

Table S3. Adsorption energies (eV) of *O, *OH and *OOH on the different sites of LSNMR, ESSI values (V) and calculated overpotentials (V) for the OER and the ORR. The values in bold are used to determine the BI of LSNMR.

description	ΔG_O	ΔG_{OH}	ΔG_{OOH}	$ESSI_{OER}$	η_{OER}	$ESSI_{ORR}$	η_{ORR}
Ni@LSNMR	3.71	1.47	4.41	0.62	1.01	-0.62	0.72
Mn@LSNMR	3.12	0.96	4.08	0.93	0.93	**-0.31**	**0.39**
Ru@LSNMR	2.27	0.54	3.89	**0.44**	**0.50**	-0.44	0.69

In Figure S13 we provide the correlation between $\Delta ESSI = ESSI_{OER} - ESSI_{ORR}$ and BI for Ru, Ni and Mn sites at LSNMR, the best combination of those made from Mn sites for the ORR and Ru sites for the OER, and additional data from the literature for other oxides: RuO_2,[16] IrO_2,[16] MnO_x,[16] Co_xO_y,[16, 21] and Pt(111)/PtO_2.[16, 22] For Pt(111) we extrapolated the data in ref.[22] from the fully solvated environment to the onset potential conditions where high adsorbate coverages are expected to weaken the adsorption energies of *O, *OH and *OOH at least by ~0.4, 0.19 and 0.17 eV. Following the surface Pourbaix

diagrams, for Co_xO_y we used the OER data for CoOOH and the ORR data for Co_3O_4. Likewise, for MnO_x we used the OER data for MnO_2 and the ORR data for Mn_2O_3. The mean absolute error (MAE) between the linear fit and the data is only 0.10 V. The experimental data in the inset of Figure 4 in the main text was taken from this study for LSNMR and from various references for the other materials (RuO_2,[23-24] MnO_x,[24] Pt/C,[25] IrO_2,[25] Co_yO_x[23]).
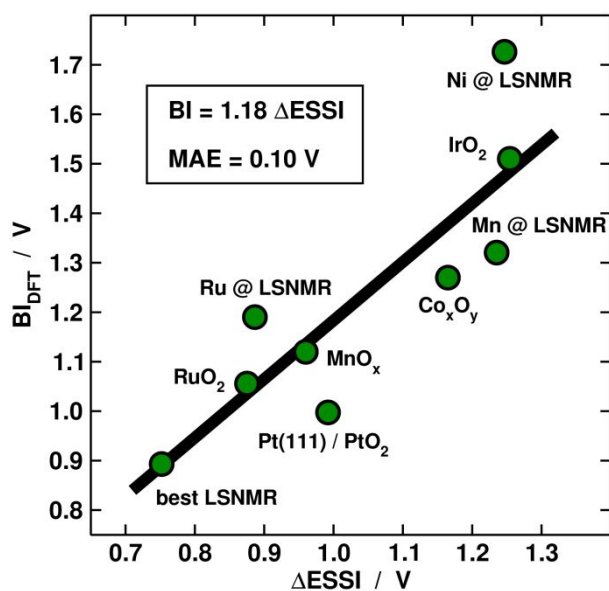
Figure S13. Correlation between ΔESSI and the DFT-calculated BI for several electrocatalysts in this study and the literature (see this SI for the data sources).

S8. Post Mortem TEM Study

S8.1. Postmortem ORR study
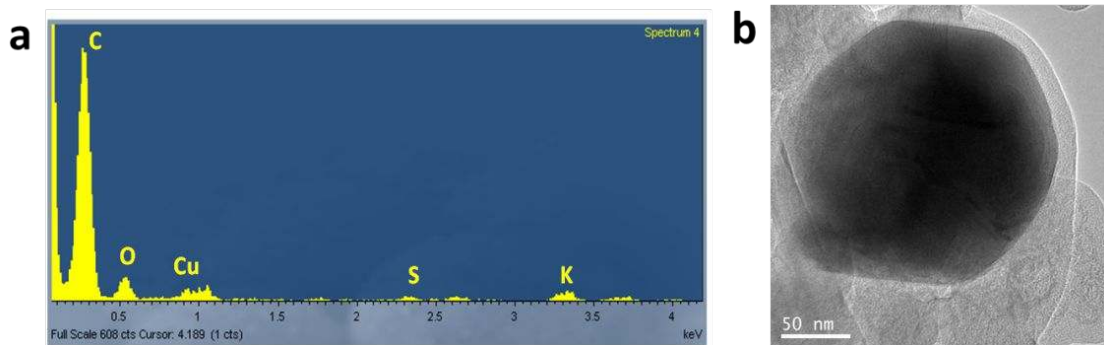
Figure S14. a) EDX of the amorphous regions around the perovskite particles. b) TEM of a particle covered by carbon.

S8.2. Postmortem OER study
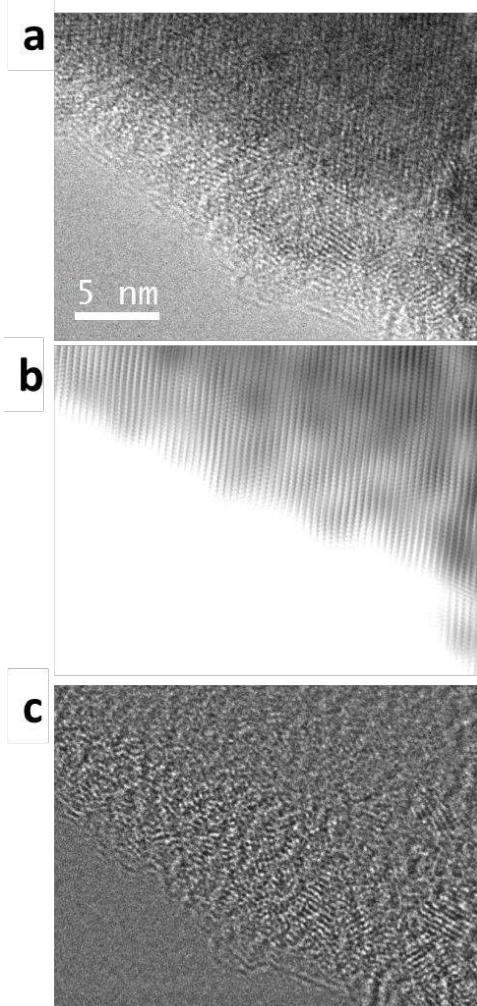
Figure S15. a) HR-TEM image of an isolated degraded particle after 500 OER cycles. b) FFT filtered image of the HR-TEM using only the reflections corresponding to the perovskite, showing that the periodicity of the structure is maintained in the bulk, and c) filtered image of the HR-TEM with the rest of reflections, indicating the presences of nanoparticles and high disorder mainly at 5-10 nm in the surface.

References

1.   Sahiner, A.; Croft, M.; Guha, S.; Perez, I. I.; Zhang, Z.; Greenblatt, M.; Metcalf, P. A.; Jahns, H.; Liang, G., Polarized Xas Studies of Ternary Nickel Oxides. *Phys Rev B Condens Matter.* **1995,** *51* (9), 5879-5886.

2.   Mandal, T. K.; Croft, M.; Hadermann, J.; Van Tendeloo, G.; Stephens, P. W.; Greenblatt, M., La$_2$MnVO$_6$ Double Perovskite: a Structural, Magnetic and X-ray Absorption Investigation. *Journal of Materials Chemistry* **2009,** *19* (25), 4382.

3.   Bune, R. O.; Lobanov, M. V.; Popov, G.; Greenblatt, M.; Botez, C. E.; Stephens, P. W.; Croft, M.; Hadermann, J.; Tendeloo, G. V., Crystal Structure and Properties of Ru-Stoichiometric LaSrMnRuO$_6$. *Chem. Mater.* **2006,** *18*, 2611-2617.

4.   Retuerto, M.; Li, M.-R.; Go, Y.; Ignatov, A.; Croft, M.; Ramanujachary, K.; Hadermann, J.; Hodges, J.; Herber, R.; Nowik, I., Magnetic and Structural Studies of the Multifunctional Material SrFe$_{0.75}$Mo$_{0.25}$O$_{3-\delta}$. *Inorganic chemistry* **2012,** *51* (22), 12273-12280.

5.   Groot, F. M. F. d.; Z. W. Hu; Lopez, M. F.; Kaindl, G.; Guillot, F.; Tronc, M., Differences Between L$_3$ and L$_2$ X-Ray Absorption Spectra of Transition Metal Compounds. *J. Chem. Phys.* **1994,** *101* (8), 6570-6576.

6.   Hu, Z.; Lips, H. v.; Golden, M. S.; Fink, J.; Kaindl, G.; Groot, F. M. F. d.; Ebbinghaus, S.; Reller, A., Multiplet Effects in the Ru-L$_{2,3}$ X-Ray Absorption Spectra of Ru(IV) and Ru(V) Compounds. *Physical Review B* **2000,** *61* (8), 5262.

7.   McCrory, C. C.; Jung, S.; Peters, J. C.; Jaramillo, T. F., Benchmarking Heterogeneous Electrocatalysts for the Oxygen Evolution Reaction. *J Am Chem Soc* **2013,** *135* (45), 16977-87.

8.   Kresse, G.; Furthmüller, J., Efficient Iterative Schemes for Ab Initio Total-Energy Calculations Using a Plane-Wave Basis Set. *Physical Review B* **1996,** *54* (16), 11169-11186.

9.   Kresse, G.; Joubert, D., From Ultrasoft Pseudopotentials to the Projector Augmented-Wave Method. *Physical Review B* **1999,** *59* (3), 1758-1775.

10.   Perdew, J. P.; Burke, K.; Ernzerhof, M., Generalized Gradient Approximation Made Simple. *Physical Review Letters* **1996,** *77* (18), 3865-3868.

11.   Dudarev, S. L.; Botton, G. A.; Savrasov, S. Y.; Humphreys, C. J.; Sutton, A. P., Electron-Energy-Loss Spectra and the Structural Stability of Nickel Oxide: An LSDA+U study. *Physical Review B* **1998,** *57* (3), 1505-1509.

12.   Zhou, F.; Cococcioni, M.; Marianetti, C. A.; Morgan, D.; Ceder, G., First-Principles Prediction of Redox Potentials in Transition-Metal Compounds With LDA+U. *Physical Review B* **2004,** *70* (23), 235121.

13.   Xu, Z.; Rossmeisl, J.; Kitchin, J. R., A Linear Response DFT+U Study of Trends in the Oxygen Evolution Activity of Transition Metal Rutile Dioxides. *J. Phys. Chem. C* **2015,** *119* (9), 4827-4833.

14.   Calle-Vallejo, F.; Inoglu, N. G.; Su, H.-Y.; Martínez, J. I.; Man, I. C.; Koper, M. T. M.; Kitchin, J. R.; Rossmeisl, J., Number of Outer Electrons as Descriptor for Adsorption Processes on Transition Metals and Their Oxides. *Chemical Science* **2013,** *4* (3), 1245.

15.   Calle-Vallejo, F.; Díaz-Morales, O. A.; Kolb, M. J.; Koper, M. T. M., Why Is Bulk Thermochemistry a Good Descriptor for the Electrocatalytic Activity of Transition Metal Oxides? *ACS Catal.* **2015,** *5* (2), 869-873.

16.   Man, I. C.; Su, H.-Y.; Calle-Vallejo, F.; Hansen, H. A.; Martinez, J. I.; Inoglu, N. G.; Kitchin, J.; Jaramillo, T. F.; Norskov, J. K.; Rossmeisl, J., Universality in Oxygen Evolution Electrocatalysis on Oxide Surfaces. *ChemCatChem* **2011,** *3* (7), 1159-1165.

17.   Briquet, L. G. V.; Sarwar, M.; Mugo, J.; Jones, G.; Calle-Vallejo, F., A New Type of Scaling Relations to Assess the Accuracy of Computational Predictions of Catalytic Activities Applied to the Oxygen Evolution Reaction. *ChemCatChem* **2017,** *9* (7), 1261-1268.

18.   Nørskov, J. K.; Rossmeisl, J.; Logadottir, A.; Lindqvist, L.; Kitchin, J. R.; Bligaard, T.; Jónsson, H., Origin of the Overpotential for Oxygen Reduction at a Fuel-Cell Cathode. *J. Phys. Chem. B* **2004,** *108* (46), 17886-17892.

19.   Calle-Vallejo, F.; Koper, M. T. M., First-Principles Computational Electrochemistry: Achievements and Challenges. *Electrochimica Acta* **2012,** *84*, 3-11.

20.   Govindarajan, N.; García-Lastra, J. M.; Meijer, E. J.; Calle-Vallejo, F., Does the Breaking of Adsorption-Energy Scaling Relations Guarantee Enhanced Electrocatalysis? *Current Opinion in Electrochemistry* **2018,** *8*, 110-117.

21.   Bajdich, M.; García-Mota, M.; Vojvodic, A.; Nørskov, J. K.; Bell, A. T., Theoretical Investigation of the Activity of Cobalt Oxides for the Electrochemical Oxidation of Water. *J. Am. Chem. Soc.* **2013,** *135* (36), 13521-13530.

22.   Calle-Vallejo, F.; Tymoczko, J.; Colic, V.; Vu, Q. H.; Pohl, M. D.; Morgenstern, K.; Loffreda, D.; Sautet, P.; Schuhmann, W.; Bandarenka, A. S., Finding Optimal Surface Sites on Heterogeneous Catalysts by Counting Nearest Neighbors. *Science* **2015,** *350* (6257), 185.

23.   Masa, J.; Xia, W.; Sinev, I.; Zhao, A.; Sun, Z.; Grützke, S.; Weide, P.; Muhler, M.; Schuhmann, W., Mn_xO_y/NC and Co_xO_y/NC Nanoparticles Embedded in a Nitrogen-Doped Carbon Matrix for High-Performance Bifunctional Oxygen Electrodes. *Angewandte Chemie International Edition* **2014,** *53* (32), 8508-8512.

24.   Su, H.-Y.; Gorlin, Y.; Man, I. C.; Calle-Vallejo, F.; Nørskov, J. K.; Jaramillo, T. F.; Rossmeisl, J., Identifying Active Surface Phases for Metal Oxide Electrocatalysts: a Study of Manganese Oxide Bi-Functional Catalysts for Oxygen Reduction and Water Oxidation Catalysis. *Phys. Chem. Chem. Phys.* **2012,** *14* (40), 14010-14022.

25.   Aijaz, A.; Masa, J.; Rösler, C.; Xia, W.; Weide, P.; Botz, A. J. R.; Fischer, R. A.; Schuhmann, W.; Muhler, M., $Co@Co_3O_4$ Encapsulated in Carbon Nanotube-Grafted Nitrogen-Doped Carbon Polyhedra as an Advanced Bifunctional Oxygen Electrode. *Angewandte Chemie International Edition* **2016,** *55* (12), 4087-4091.